Results in Engineering 18 (2023) 101166

Contents lists available at ScienceDirect

Results in Engineering

journal homepage: www.sciencedirect.com/journal/results-in-engineering

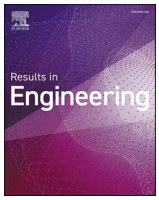

Analysis of the local growth and density evolution of soot deposits generated under hydrocarbon condensation: 3D simulation and detailed experimental validation

Jesús Vence, Concepción Paz *, Eduardo Suárez, Adrián Cabarcos, Miguel Concheiro

CINTECX, Universidade de Vigo, Campus Universitario Lagoas-Marcosende, 36310, Vigo, Spain

ARTICLE INFO

Keywords:
HC
Soot
Condensation
Fouling
EGR

ABSTRACT

The utilization of the Exhaust Gas Recirculation (EGR) system during atypical engine operating conditions in order to meet future type-approval criteria exposes the internal surfaces of the devices to exhaust gas with elevated concentrations of particulate matter and greater amounts of hydrocarbon species, leading to the formation of dense and wet sludge deposits. To broaden the understanding of this phenomenon and contribute to the development of advanced EGR devices, this study presents an extended Computational Fluid Dynamics (CFD) model that, in addition to simulating the growth of fouling deposits caused by the accumulation of soot particles, also takes into account the condensation of hydrocarbons. Two scenarios with varying hydrocarbon concentrations in the exhaust flow are analysed, and the evolution of the deposit's thickness and density is determined. A sequential validation process is carried out by comparing the numerical results to actual deposit profiles at different stages of the fouling process. Additionally, hyperspectral images of the fouling layer have been acquired and analysed to validate the regions where hydrocarbon condensation is predicted to play a crucial role, enabling the verification of the hydrocarbon condensation phenomenon predicted by the numerical model. The results obtained under the studied conditions indicate that, on average, 77.4% of the analysed area exhibits a low level of relative error, demonstrating that the proposed model and the methodology used serve as a valuable tool for examining the propensity for deposit formation in devices subjected to fouling exacerbated by hydrocarbon condensation.

1. Introduction

The increasing awareness about climate change and its undesirable effects is forcing national governments to develop new environmental standards to reduce greenhouse gas emissions, especially those generated by road traffic. That is why European Commission has planned a drastic reduction of the emission of new passenger cars by 2030, requiring automotive manufacturers to use the best technology available and to search and implement greener technologies [1,2]. The electrification of powertrains, the use of biofuels or the employment of dual fuel concepts are currently the most viable options to meet the new rigorous standards in transport sector [3–6]. Although battery electric vehicles (BEVs) are the most popular alternative to fossil fuels, they have some shortcomings at present, such as long battery charging times, higher manufacturing cost than current vehicles or lower power density than traditional automobiles [7,8]. In this context, the use of internal combustion engines in hybrid-electric vehicles, which are commonly fuelled with gasoline, the adoption of biofuels, or even the implementation of dual fuel modes of operation, like the injection of compressed natural gas (CNG) or hydrogen as supplementary fuels, provide significant emission reductions, positioning these options as attractive solutions for light- and heavy-duty vehicles in the upcoming years [9–14].

Current emission regulation in Europe, Euro 6-E, and the future potential Euro 7, expected to come into force on 2025, include more stringent restrictions to the nitrogen oxides (NO_x) and Particulate Matter (PM) emissions. Although the full extent of the future law is not clear yet, some previous studies have presented different predictions, anticipating that the limit of NO_x emissions will be around 0.2 g/kWh and that vehicles will be tested under the in-service conformity procedure, in order to guarantee that the real emissions are within the range allowed

* Corresponding author.
E-mail addresses: jvence@uvigo.es (J. Vence), cpaz@uvigo.es (C. Paz), suarez@uvigo.es (E. Suárez), acabarcos@uvigo.es (A. Cabarcos), mconcheiro@uvigo.es (M. Concheiro).

https://doi.org/10.1016/j.rineng.2023.101166
Received 15 March 2023; Received in revised form 26 April 2023; Accepted 12 May 2023
Available online 13 May 2023

throughout their normal life [15–17].

Under this scenario, the Exhaust Gas Recirculation (EGR) system, one of the widely accepted technology in charge of reduce the NO_x production, needs to extend its typical operating range, adapting its performance toward a broader range of operative and environmental conditions to meet the future type-approval criteria [18–20]. The use of the EGR system under unusual engine operating conditions, such as the cold-start phase or incomplete combustion events, that produce largely critical amounts of pollutant emissions, leads to exposure of the internal surfaces of the devices to exhaust gas flows with higher concentrations of particulate matter and greater quantities of volatile and hydrocarbon (HC) species [21–23]. These operating conditions significantly increase the fouling phenomenon that takes place throughout the EGR system and, more importantly, on the heat exchanger surfaces of the EGR cooler. For this reason, the wider operating range of the EGR system resulted from the Real Driving Emissions (RDE) tests, has provided relevant insights for the analysis of the fouling process produced under high HC concentrations.

The study of the fouling phenomenon produced by the deposition of soot particles and the condensation of HC species has traditionally been addressed in two ways: one group have analysed the fouling process employing experimental approaches, i.e., carrying out in-situ measurements to determine the growth of the deposit and to evaluate the morphology and properties of the fouling layer, while the second group have employed numerical approaches to recreate the deposit formation and its specific characteristics.

On the one hand, several studies were focused on the analysis of fouling layers from an experimental perspective to obtain an in-depth understanding of deposits produced under the new operating range of the EGR system. Tanaka et al. [24,25] evaluated the EGR fouling formation mechanisms based on Attenuated Total Reflection Fourier Transform Infrared spectrometry (ATR-FTIR) and spatially- and time-resolved Scanning Electron Microscopy (SEM) techniques. Measuring deposits that were generated in a custom-made sample line employing different real diesel engine exhaust flows, they detected that two types of deposits can be formed: hard deposits, that presented high concentrations of polycyclic aromatic hydrocarbons (PAHs), with more than twenty carbon atoms, and that had a dense structure and no voids; and powdery deposits, whose internal structure presented a “grape-like” shape with voids such as the particulate matter. In the same vein, Sakaida et al. [26], through a Gas Chromatography Mass Spectrometry (GCMS) analysis evaluated deposits produced under different exhaust gas compositions, determining that the PAHs concentration in the exhaust flow can significantly increase the hard deposit formation. Similarly, Reza Razmavar and Reza Malayeri [27] assessed how condensation of hydrocarbons and water can impact on deposit formation inside EGR coolers. Injecting water and icosane ($C_{20}H_{42}$), they observed that, when condensation occurs prior to soot deposition, condensed HC can roll over the heat exchange surface, moving away the soot particles and not allowing them to build up the deposit. They verified that coolant temperature can have a relevant effect on HC condensation process, estimating that lowering coolant temperature from 90 °C to 25 °C can reduce 60% the thermal resistance of fouling. In a parallel effort, they analysed the condensation of water vapour, determining that water droplets can assist the removal phenomenon, causing a partial fouling layer flake-off and, consequently, mitigating the EGR cooler fouling to some extent.

On the other hand, recent studies developed numerical approaches with the aim of reproduce and simulate the deposition of particulate matter and the condensation of volatile species of the EGR flow. In this sense, Galindo et al. [28] presented 3D Computational Fluid Dynamics (CFD) simulations that quantify the water condensation produced in three-way EGR mixers during the engine warm-up and at cold ambient conditions. These simulations, which were enhanced with a condensation submodel, predicted the main flow features inside different junctions under various operating conditions, allowing the evaluation of the condensed water mass fraction and the regions of the EGR mixer where condensation takes place. The numerical outcomes of this study were validated using two distinct optical methodologies: Particle Image Velocimetry (PIV) and laser-induced visualization, demonstrating a substantial concurrence between the numerical and experimental results. In accordance with this perspective, Liebsch et al. [29] established a one-dimensional simulation model to evaluate the fouling rate of the EGR coolers considering different engine operating points. Utilizing a thorough experimental analysis of the concentration and boiling temperature ranges of various HC species, this numerical tool assessed the fouling risk of the EGR cooler considering the engine map, enabling the identification of the engine operating ranges that exhibit higher fouling tendencies.

Despite recent studies’ endeavours to develop comprehensive numerical models to assess the fouling occurrence within the EGR system under diverse operating conditions, the literature review conducted by Paz et al. [30] revealed that there are only a limited number of numerical models that accurately simulate the actual deposit growth considering the local-scale effects involved in the fouling process. Some models, such as the 2-D axisymmetric model proposed by Abarham et al. [31], have the capacity to recreate the local progression of the fouling deposits resulting from particulate matter deposition. However, there is currently no numerical approach that integrates the local evolution of the fouling layer taking into account both particulate matter accumulation and HC condensation.

Given this context, to contribute to the design of novel devices adjusted to the new requirements of the EGR technology, the aim of this study is to extend a simulation model to reproduce the growth of the fouling layer, which are not only produced by the accumulation of soot particles but also generated due to the condensation of HCs. This study leverages validated numerical techniques previously presented in the literature [32,33], which solely account for the production of deposits resulting from the aggregation of particulate matter, and extends them into a new simulation strategy that incorporates the local calculation of the condensation of hydrocarbons during the fouling layer formation process. The model’s results were evaluated by comparing the model-predicted deposit topography with experimental measurements, computing local errors. Furthermore, to validate the regions where HC condensation is predicted to play a crucial role, hyperspectral images of the fouling layers were captured and analysed, enabling a comparison of chemical colour images and numerical results.

2. Numerical methodology

2.1. Numerical model

This section outlines the new extended numerical model, which takes into account the effect of HC condensation on the growth of the deposit, developed on the foundation of a prior numerical methodology [32,33]. The key equations, particularly those related to the condensation of volatile species, and the adopted technique are thoroughly presented below.

On the one hand, to reproduce the evolution of the fouling layer due to the accumulation of particulate matter, this model adopted the broad accepted strategy that combines the deposition and the removal of particles as two opposing and simultaneous processes [34–36]. The particulate matter deposition was modelled by considering the drift velocity caused by thermophoretic force (V_{th}), computing the modified Cha-McCoy-Wood correlation [37,38]. Moreover, the model took into account the drift velocity due to diffusion transport (V_d), turbulent impaction and inertial effects (V_t), that was evaluated employing the Wood empirical correlation [39]. The particle removal was calculated by considering the shear force (τ_w). Taking into consideration the balance between the forces action on a particle resting on a flat surface, the particle removal flux was computed employing the strategy proposed by Warey et al. [40].

The sticking probability (S)–the fraction of the particulate matter approaching the surface that will adhere to the deposit–was computed evaluating the force balance between the drag (F_d) and adhesion (F_{adh}) forces [41,42]. If the adhesion force that act on a particle is greater than the drag force, the particle will rest on the deposit and the sticking probability will be $S = 1$.

On the other hand, when the upper surface of the fouling layer is below the dew point of HC species, they can condense, becoming part of the deposit. The mass transfer phenomenon that takes place when condensation occurs involves the molecules of the vapour specie that form droplets that are added to the deposit and, considering the local partial pressure of each compound in the main flow and at the interface of the fouling layer, the mass condensation flux from the exhaust gas stream to the deposit was computed as [43]:

$$j_{g,i} = K_g \rho_g \ln\left(\frac{1 - y_{g,i}}{1 - y_{g,o}}\right) \quad [1]$$

where $y_{g,i}$ and $y_{g,o}$ are the mole fraction of the HC specie in the gas-liquid interface and in the exhaust flow, respectively, ρ_g is the density of the exhaust gas and K_g represents the mass transfer coefficient, that is calculated as [43]:

$$K_g = \left(\frac{h_g}{\rho_g C_{p,g}}\right)\left(\frac{Pr}{Sc}\right)^{\frac{2}{3}} \quad [2]$$

where h_g is the heat transfer coefficient, $C_{p,g}$ is the heat capacity of the exhaust gas and Pr and Sc represent the Prandtl number and the Schmidt number, respectively. The mole fraction of each specie in the gas-fouling interface was computed as the coefficient between the partial pressure at the upper surface of the deposit ($P_{g,i}$) and the total pressure of the gas flow (P_{total}) as [44]:

$$y_{g,i} = \frac{P_{g,i}}{P_{total}} \quad [3]$$

The partial pressure of the HC species (mmHg) was determined employing the Antoine coefficients of each compound [44]:

$$\log_{10} P_{g,i} = A - \frac{B}{T_{interface} + C} \quad [4]$$

In this manner, for a particular HC concentration on the fouling-gas interface, $T_{interface}$ (°C) indicates the threshold level of temperature below which HC condensation takes place.

Previous research have reported that, when the deposit is generated due to the accumulation of particulate matter and the condensation of HC, fouling exhibits a stratified structure [45,46]. The base sublayers of the deposit, that are generated during the early stages of the deposit formation when HC condensation is more persistent, show a denser structure, derived from the combination of the deposition of agglomerates and the condensation of HC on the fouling layer [47]. HC condensates fill the porous structure of the deposit, changing its internal configuration from dry deposit–with low density–to slurry-type fouling layer–with higher density [48–50].

In order to incorporate the impact of HC condensation on the internal structure of the fouling deposit, this study modelled the deposit growth as a heterogeneous deposit with non-uniform density. When there was no HC condensation, the fouling layer was calculated based on the deposit having a porous structure, with a density of 42.5 kg/m^3, in line with previous experimental findings [47,51,52]. Conversely, when the top surface of the deposit was below the dew point of the HCs and condensation took place, the deposit growth was calculated to result in a denser fouling layer. Consistent with prior experimental measurements, under HC condensation, the deposit density can be up to twice as high and the fouling density can reach values close to 100 kg/m^3 [47].

At each time-step of the simulation, once the fluid field was computed, the numerical model calculated the local thickness of the deposit (Δx_f) combining the equations of the accumulation of particulate matter and the criterion of the selection of the fouling layer density according to the HC condensation phenomenon:

$$\Delta x_f = \left(\frac{S\,(V_{th} + V_d + V_t)\,C}{\rho_f} - K\tau_w x_f\right)\Delta t \quad [5]$$

where C represents the particle concentration and K refers to a removal proportionality constant (2×10^{-6}), that was fitted with our experimental data. Subsequently, the dynamic mesh model was utilized to update the computational domain, reproducing the actual growth of the deposit.

This numerical strategy, as depicted in Fig. 1, allowed the evaluation of the HC condensation effect. It calculated the HC dew temperature based on the HC concentration at the fouling-gas interface and then used this information to determine the local HC condensation flow and local fouling layer density of each sublayer of the deposit. As shown in Fig. 1b, under HC concentration of 949 ppm of hexadecane ($C_{16}H_{34}$), the model determined that the local HC condensation flow could reach 0.042 mg/s at a local temperature of 46.5 °C at the fouling-gas interface. However, when the HC concentration was reduced to half (474 ppm of $C_{16}H_{34}$), the HC condensation flow was only 0.013 mg/s at the same local temperature. Fig. 1c illustrates that the addition of HC condensate to the deposit altered the total local fouling density, resulting in denser fouling layers in areas where condensation was more persistent during the fouling process.

2.2. Boundary conditions and simulation setup

In order to assess the predictive capabilities of the new numerical method, the different fouling processes presented in the study of Paz et al. [47] were reproduced.

As at the previous study, the test section was based on a rectangular channel with an inlet hydraulic diameter of 13.97 mm with a ribbed plate with 11 ribs of 3.25 mm high, on which the deposit built up.

To evaluate the effect of HC condensation during the fouling layer formation, hexadecane ($C_{16}H_{34}$) was employed, since it is one of the major alkane species in diesel deposits [53–58].

Table 1 summarises the two different scenarios that were reproduced: HC-50, that considered a hexadecane injection of 50 μl/min–equivalent to a hexadecane mole fraction of 2.966×10^{-5}–, and HC-100, that considered a hexadecane injection of 100 μl/min–equivalent to a hexadecane mole fraction of 5.932×10^{-5}–. To evaluate the different stages of the fouling process, simulations were performed for 3, 6, and 9 h durations.

Based on the results of a prior grid-independent study [33], the meshes were generated with a cell size of 0.5 mm. The final 3D cell count for the entire assembly was approximately 8×10^6 cells.

The simulations were performed employing Ansys Fluent 2020 R2 CFD software. The k-ε turbulence model, which is based on a RANS-based modelling approach, was selected and the enhanced near wall treatment method was adopted. Due to the operating conditions of this study present low Mach number, the incompressible-ideal-gas law was used to compute the gas density variations according to the flow temperature. A pressure-based solver and a Semi-Implicit Method for Pressure-Linked Equations (SIMPLE) pressure-velocity coupling were adopted and, to compute the turbulence, momentum and energy equations, the Quadratic Upwind Interpolation for Convection Kinematics (QUICK) scheme was employed.

In order to evaluate the convergence of the simulations, both scaled residuals and various key parameters of the gas flow, such as the temperature and velocity at different positions of the geometry, were monitored. At each time-step of the simulation, the convergence criterion was established upon the attained of scaled residuals lower than 10^{-3} for all variables, in accordance with the recommended Fluent convergence criterion [59].

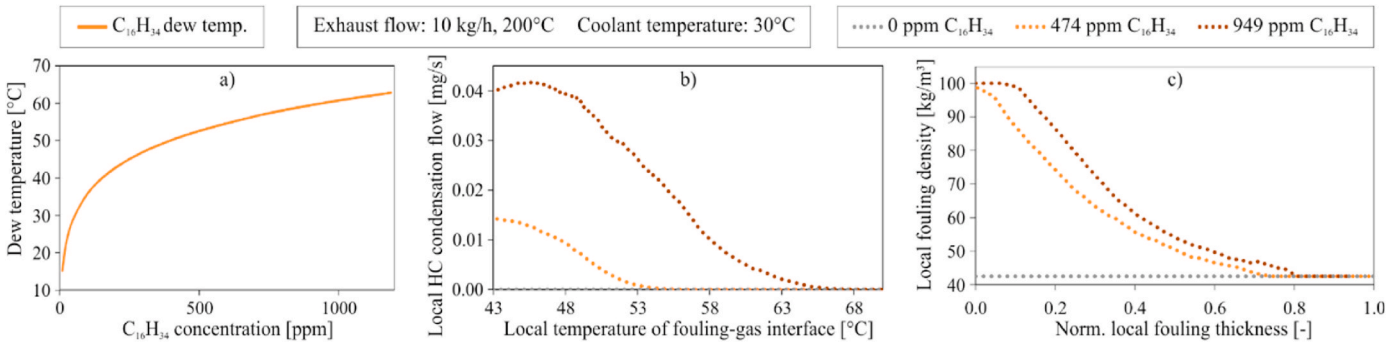

Fig. 1. Early outcomes of the numerical model: (a) dew temperature of hexadecane ($C_{16}H_{34}$), (b) local HC condensation flow, and (c) local fouling layer density computed by the numerical model.

Table 1
Boundary conditions of the simulations.

	Test duration [h]	Exhaust gas flow rate [kg/h]	Exhaust gas temperature [°C]	$C_{16}H_{34}$ injection flow [μl/min]	Coolant temperature [°C]
HC-50	3	10	200	50	30
	6	10	200	50	30
	9	10	200	50	30
HC-100	3	10	200	100	30
	6	10	200	100	30
	9	10	200	100	30

3. Results and model validation

In this section, the results obtained using the new wet fouling model are presented. To evaluate the suitability and improvements offered by this model compared to previous strategies that neglected the hydrocarbon condensation phenomenon, the first section provides a comparison of the results obtained with the new approach versus those obtained using previous models. Then, a detailed validation of the results against experimental data is provided. Finally, the results concerning the evolution of the deposit density calculated using the new simulation model are presented.

3.1. Simulation of the fouling process considering HC condensation

To assess the suitability of the equations and criterions selected in the HC condensation model, Fig. 2 shows a comparative analysis between the results of the CFD model neglecting the effect of HC condensation–previous dry fouling model–and the numerical results

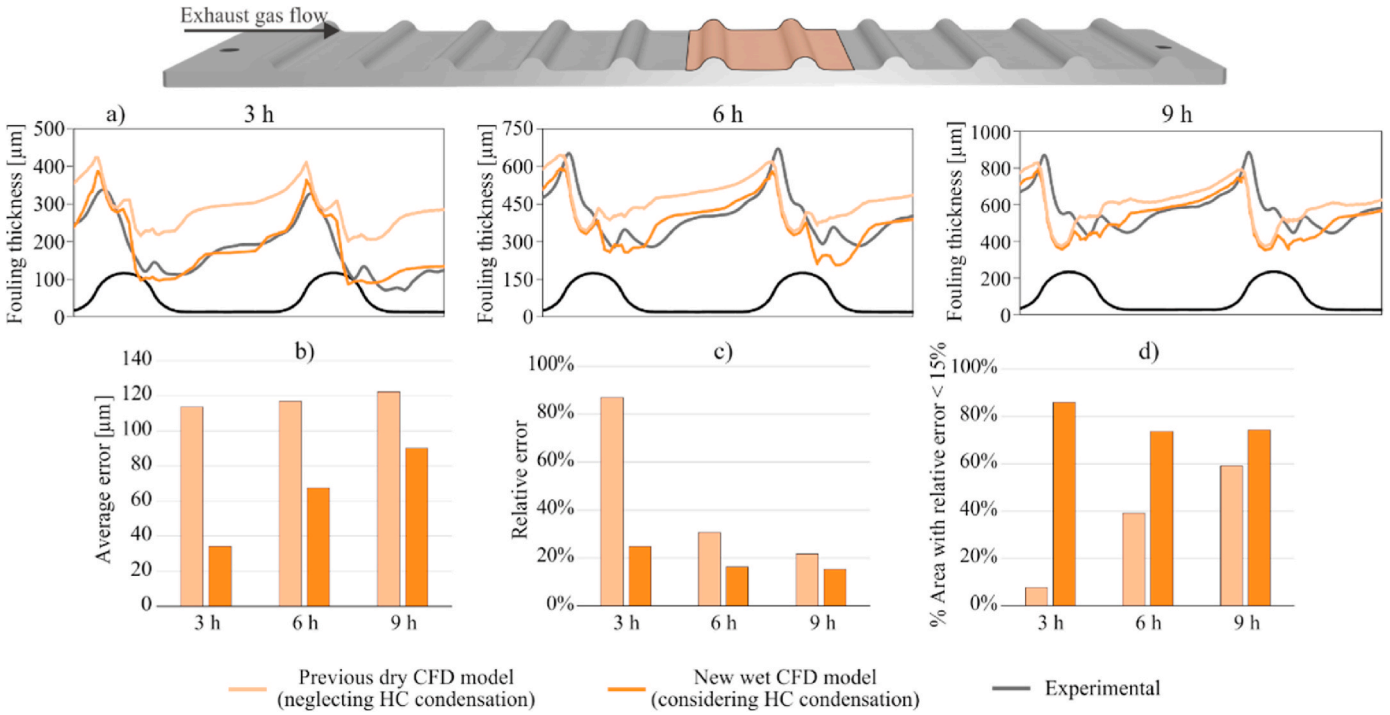

Fig. 2. *CFD results of both previous dry CFD model and new wet CFD model, as well as experimental data [47] of case HC-50 of the 3-, 6- and 9-h tests: (a) fouling profiles, (b) average error, (c) relative error, (d) percentage of plate area with relative error less than 15%.*

considering the change of the fouling layer density produced by the HC condensate–new wet fouling model–. CFD results were compared with the experimental fouling profiles of 3-, 6-, and 9-h tests, that were obtained in our previous study [47].

Fig. 2 demonstrates that the implementation of the new numerical strategy resulted in fouling layer profiles that more closely aligned with the experimental results when HC condensation occurs. The fouling layer thickness calculated with the new wet CFD model more accurately replicated the actual deposit's shape, particularly in the early stages of the fouling formation when the layer was thin and HC condensation was more pronounced. Fig. 2b and c illustrate that the fouling thickness computed with consideration of HC condensation showed a lower deviation from the actual fouling topography. At the third hour of the fouling process, the relative error decreased from 86.9% when disregarding the effect of HC condensate to 24.7% when taking into account the fouling density associated with the HC condensation process. The improved results of the new methodology were most marked in the initial stages of deposit formation, however, the error level decreased throughout the entire fouling process, increasing the area of the plate with low relative error (<15%) from 7.6% to 85.5% after 3 h, from 39.1% to 73.7% after 6 h, and from 59.1% to 74.3% after 9 h, as depicted in Fig. 2d.

3.2. Detailed experimental validation

A sequential validation of the predictive abilities of the wet fouling model was performed by comparing the numerical results to experimental measurements at various stages of the fouling process. The numerical data was compared with the experimental results obtained in our previous study [47] after 3, 6, and 9 h of fouling layer buildup, considering the boundary conditions described in Section 2.2. Figs. 3 and 4 show the results of the CFD simulations and the experimental data for the fouling layer in case HC-50 and case HC-100, respectively.

The numerical results allowed for the calculation of the non-uniform growth of the fouling layer along the ribbed plate, showing a local maximum thickness of fouling at the foot of the incident side of each rib. This is attributed to the deposition of particulate matter, which is primarily caused by the thermophoretic force, and the limited removal effect of the exhaust flow in this region due to the low gas velocity. Consequently, this leads to a sustained growth of the deposit in this area throughout the entire process. In contrast, the rib shadow zone, being the least exposed region to the exhaust flow, exhibits the minimum local thickness, and the growth of the fouling layer in this section is less pronounced.

The analysis of the fouling topographies demonstrated a gradual decrease in the thickness of the deposit along the plate, particularly during the early stages of the fouling layer formation. The deposit profiles of cases HC-50 and HC-100 after 3 h of testing exhibited a reduction in fouling growth near the outlet section of the plate, as shown in Fig. 5. During the initial stages of deposit formation, the low temperature of the fouling-gas interface resulted in HC condensation, increasing the hydrocarbon-to-soot ratio within the deposit, and causing compaction of the deposited particulate matter, leading to the formation of thinner deposits [60,61]. This was particularly pronounced in case HC-100, which had a higher HC concentration in the exhaust gas, where at the third hour of the fouling process, the deposit displayed lower thickness in the second half of the plate, reducing the local maximum from 258 μm in the last rib of case HC-50 to 198 μm in the same position of case HC-100. As the deposit growth advanced, the reduction in HC condensation due to the increase in the temperature of the fouling-gas interface resulted in homogenization of the fouling thickness along the test probe [62]. Once HC condensation decreased or even ceased, and the addition of volatile material to the deposit was reduced, the growth of the fouling displayed a more uniform distribution along the probe. This homogenization was particularly marked in case HC-50, which had a lower HC concentration, where the lower amount of HC condensate had a lesser impact on the fouling layer formation near the outlet region of the heat exchanger.

The analysis of the local evolution of the deposit indicated that, although the majority of the surface of the plate experienced sustained growth as the test progressed, the fouling layer thickness of the regions located on the upper section of the windward side of the ribs approached an asymptotic value after 9 h of testing. As demonstrated by points 3 and 4 in Fig. 5, a slowdown in deposit growth was observed during the final 3 h of the test, causing the fouling layer thickness to change only slightly, from 412 to 441 μm on point 3 of Section A from the sixth to the ninth hour. Additionally, it was noted that in this region, the concentration of HC in the exhaust gas had little impact on the evolution of the fouling layer, as the results of cases HC-50 and HC-100 were practically the same. On the windward side of the ribs, the gas flow impacts the plate, raising the temperature of the deposits and reducing HC condensation, ensuring similar dry fouling conditions during the progressive stages of deposit formation [63–65].

The discrepancy between the experimental data and numerical

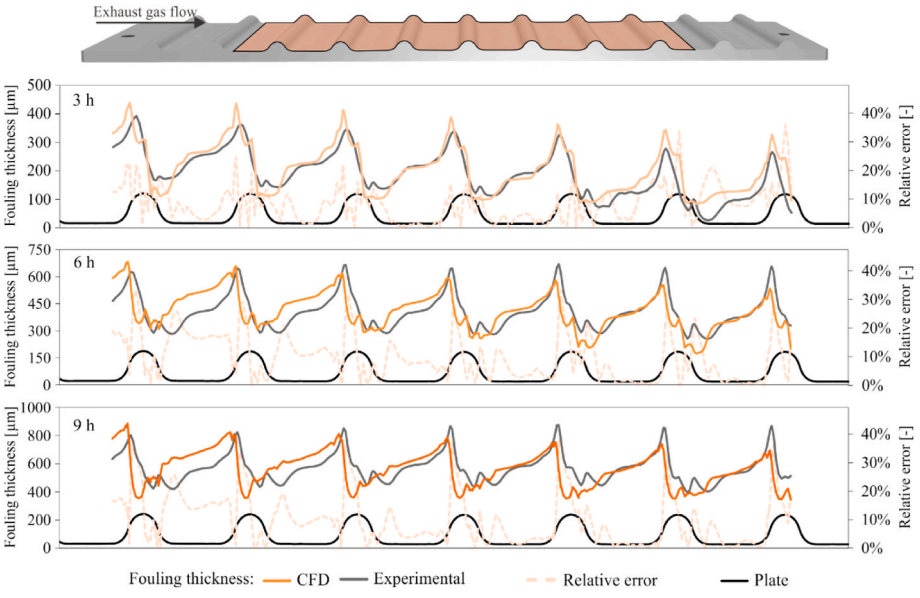

Fig. 3. *Fouling layer thickness obtained with the CFD model and experimental data* [47] *of case HC-50 of the 3-, 6- and 9-h tests.*

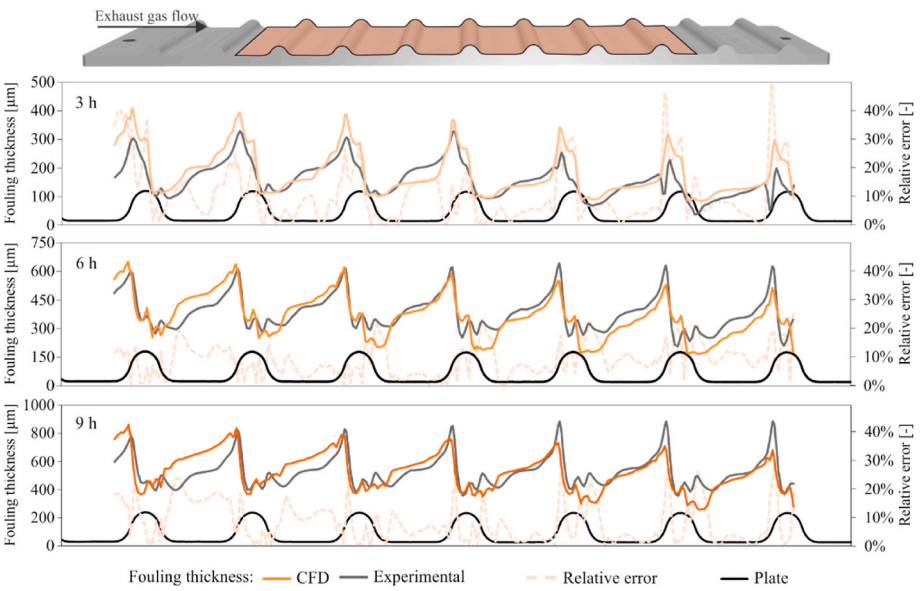

Fig. 4. *Fouling layer thickness obtained with the CFD model and experimental data* [47] *of case HC-100 of the 3-, 6- and 9-h tests.*

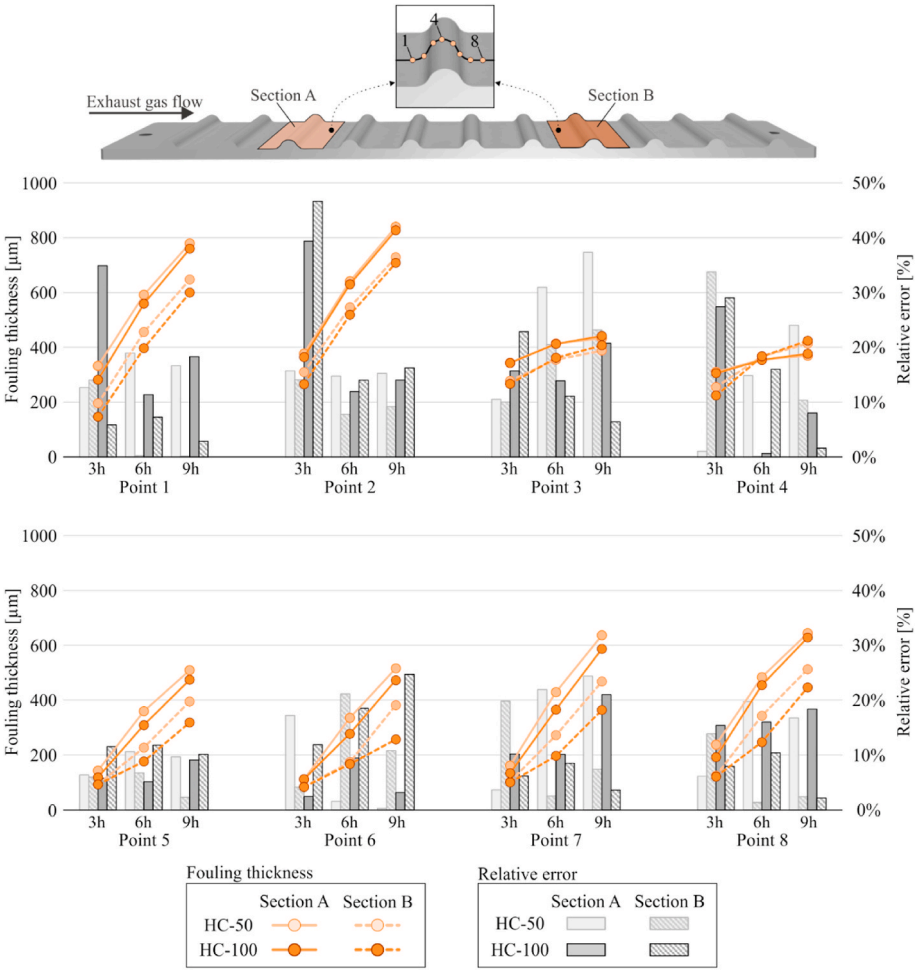

Fig. 5. Model results of fouling layer thickness (orange lines and points) and relative error (grey columns) on Points 1–8 on the plate of the 3-, 6- and 9-h tests of the cases HC-50 and HC-100. (For interpretation of the references to colour in this figure legend, the reader is referred to the Web version of this article.)

results was assessed. The average relative error for the 3-h tests was 25.1%, while the average relative errors for the 6-h and 9-h tests were 16.6% and 14.9%, respectively. As summarized in Table 2, in both scenarios the results showed a similar relative error at different stages of the fouling layer formation. This verified that the model's predictive capabilities were not affected by the changing exhaust gas conditions

Table 2
Results of cases HC-50 and HC-100 of the 3-, 6- and 9-h tests.

		Average CFD fouling thickness [μm]	Average relative error [%]	Percentage of area with error less than 15% [%]
HC-50	3 h	210.6	24.7%	85.8%
	6 h	412.7	16.4%	73.7%
	9 h	566.1	15.3%	74.3%
HC-100	3 h	186.8	25.5%	71.7%
	6 h	368.8	16.7%	82.8%
	9 h	530.2	14.5%	76.2%

produced by the increased HC concentration, and that the error remained nearly constant during different phases of deposit growth.

3.3. Fouling density evolution

The results achieved with the new numerical model allowed to analyse the evolution of the density of the deposit in a local manner. Figs. 6 and 7 show the fouling thickness and the fouling density of the deposit of the 3-, 6- and 9-h tests of the case HC-50 and the case HC-100, respectively.

The analysis of the evolution of the fouling density in the case of HC-50 showed that after the 3-h test, regions of the deposit with high density were located near the outlet section of the plate, particularly in the areas between ribs where the fouling layer was thinner. It was observed that the deposit growing in the shadow zone of the ribs in the central section of the plate also displayed the same trend–low fouling thickness and high density–. The low deposit thickness and resultant low temperature of the fouling-gas interface in these areas of the plate encouraged the HC condensation, leading to the cohesiveness of the deposit and transforming the morphology of the fouling layer from a dry porous deposit to a wet denser sludge deposit [47,52,66].

In contrast, the areas of the deposit on the windward side of the ribs that had a thicker fouling layer displayed a lower density. The rapid growth phase of the deposit in these sections during the first 3 h of the process caused a gradual increase in the temperature of the upper surface, resulting in a progressive inhibition of HC condensation and the creation of primarily dry deposits made up mostly of randomly packed and less dense particulate matter.

As the fouling layer developed over time, the density of the deposit decreased, as the results of 6-h and 9-h tests revealed. The ongoing growth of the fouling layer resulted in the creation of subsequent sublayers in the absence of condensates, resulting in a less dense structure than the base sublayers. As previously confirmed [45,67], these new sublayers within the stratified structure of the deposit are thicker than the dense base sublayers, leading to a decrease in the density of fouling, which can achieve as low density values as the areas formed in the absence of HC condensation.

The analysis of the evolution of the fouling density in the case HC-100, with higher HC concentration in the exhaust gas and a lower dew point of HC species, revealed a more pronounced impact of HC condensation on the fouling layer density. As depicted in Fig. 7, the results of case HC-100 emphasized the behaviour of the case HC-50 in the areas of the plate where HC condensation had a significant impact.

It was observed that, despite the rise in the HC concentration in the exhaust gas, due to the high temperature of the deposits located on top of the ribs, these regions were minimally impacted by HC condensation. Even after the initial stages of deposit formation, during the 3-h tests, the density in these regions remained low, suggesting that the formation of the fouling layer was a result of chaotic accumulation of dry particulate matter, resulting in a highly porous deposit.

In contrast, the deposits located on the leeward side of the final ribs were significantly impacted by HC condensation throughout the process, leading to high density even after the 9-h tests. The combination of dry soot particles and the presence of HC condensates throughout the fouling process resulted in the filling of the porous structure of the deposit, causing the formation of denser fouling layers with a slurry-like appearance in these regions over an extended period of time [68].

To validate the computed local density, hyperspectral images of the actual deposits were employed. The Specim FX17 hyperspectral camera (spectral range of 950–1700 nm and 224 spectral bands) was utilized to capture the hyperspectral images of the fouling layers of cases HC-50 and HC-100 after the 3-h tests, to assess the impact of HC condensation during the initial stages of fouling formation. As depicted in Fig. 8, the hyperspectral data cube of both deposits was compared with the spectral profile of a dry soot sample, which was generated in the absence of HC injection, and the spectral profile of a wet fouling sample, which was generated under high HC concentration. This comparison facilitated the identification of the dry fraction spectrum of the deposits, i.e., the regions with low HC content and a similar physical structure as the dry sample, and the wet fraction spectrum of the fouling layers, i.e., the regions with high HC content and a physical structure similar to the wet sample.

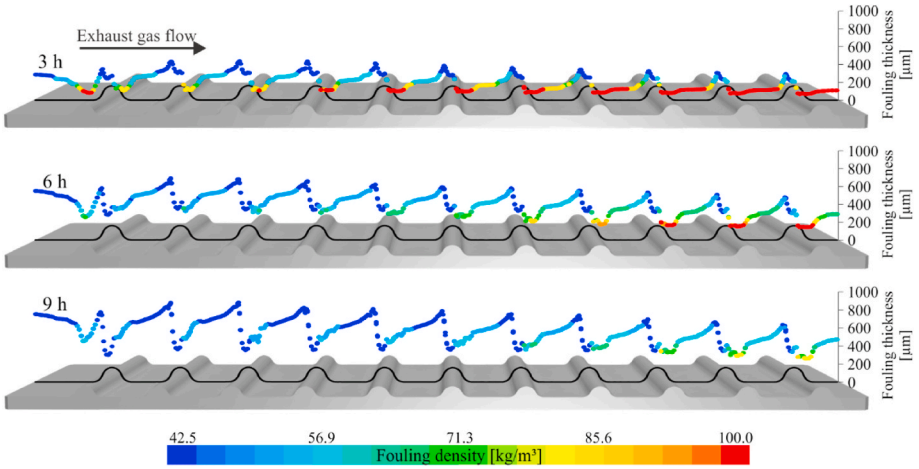

Fig. 6. Fouling thickness coloured by fouling layer density of case HC-50 of the 3-, 6- and 9-h tests.

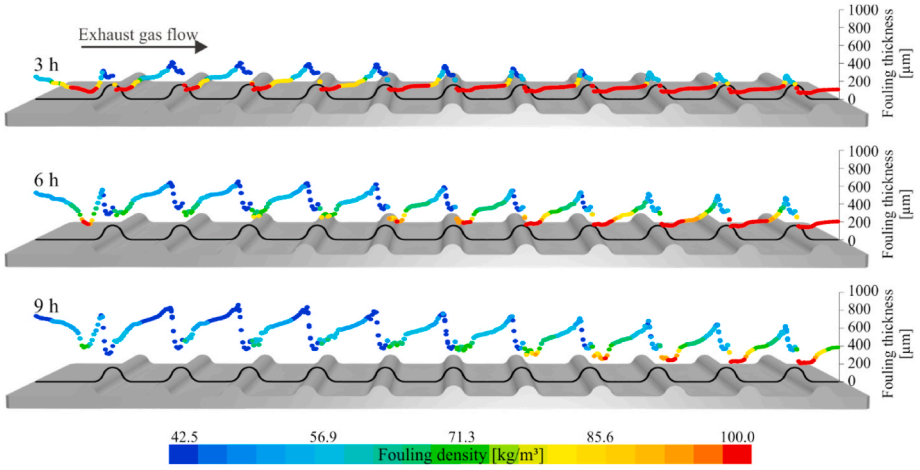

Fig. 7. Fouling thickness coloured by fouling layer density of case HC-100 of the 3-, 6- and 9-h tests.

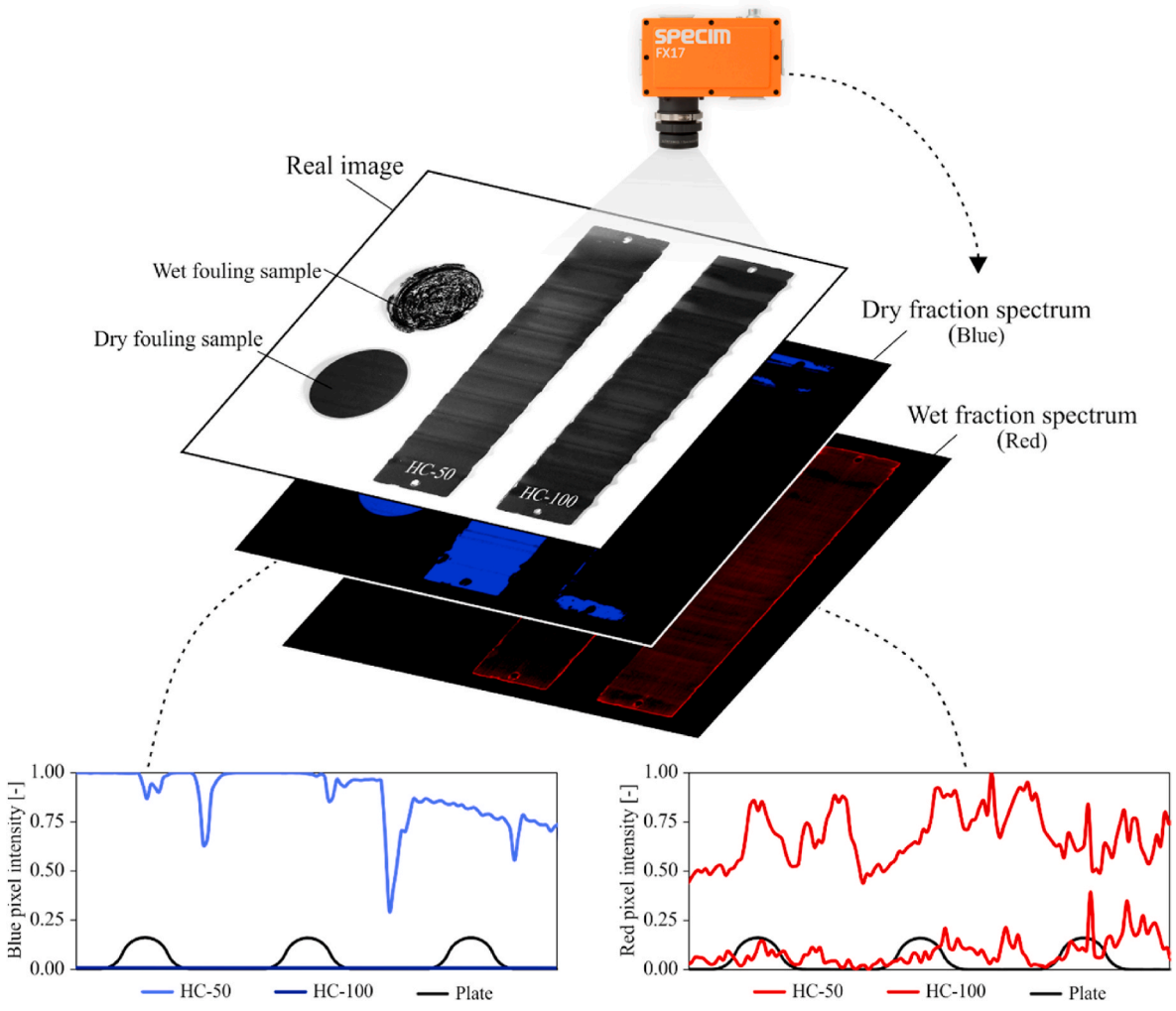

Fig. 8. Scheme of the hyperspectral image processing and graphs of the dry fraction spectrum and wet fraction spectrum of the deposits of cases HC-50 and HC-100 after 3-h tests.

Fig. 9 displays the processed hyperspectral images of the cases HC-50 and HC-100, which are color-coded according to their similarity with the dry fouling sample (represented in brown) and with the wet fouling sample (represented in orange), as well as the average wet fraction content identified along the plates in both scenarios. It was observed that the wet fraction content of the deposit of case HC-100 along the plate was higher compared to the wet fraction content of the deposit of case HC-50. This can be attributed to the higher concentration of HC in the exhaust gas flow in the case of HC-100, leading to a larger extent of HC condensation and an increase in HC content. Furthermore, it was

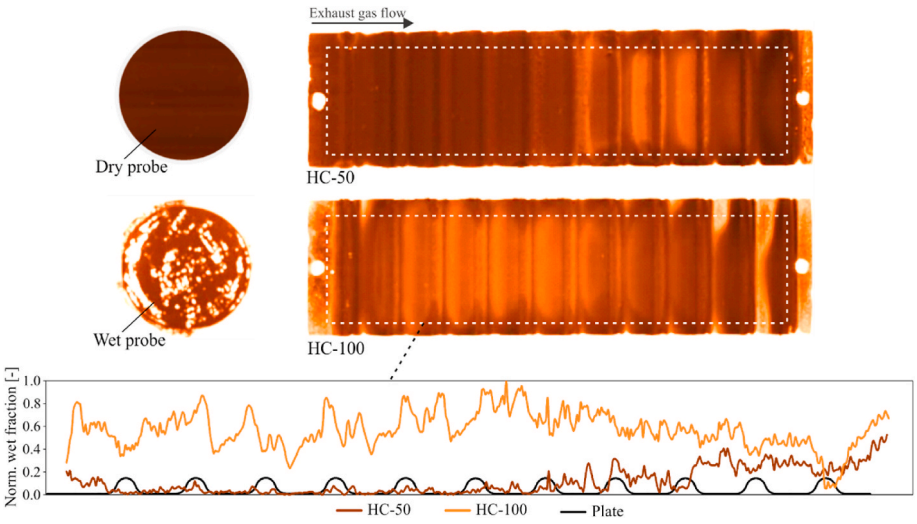

Fig. 9. Hyperspectral images of the fouling probes and plates, and graph of the normalized wet fraction of cases HC-50 and HC-100 after 3-h tests.

detected that near the outlet section of the plate, the fouling layer of case HC-50 exhibited higher wet fractions, resulting from the particularly marked HC condensation in this region.

Fig. 10 presents a comparison of the wet fraction content, which was determined through the analysis of the spectrums of the actual deposits, and the density of the deposits, which was locally computed by the numerical model. The results of the two techniques confirmed that both parameters showed a similar trend.

On the one hand, the deposit of case HC-50 displayed a noticeable rise in the fouling layer density along the plate, which was also reflected in the corresponding increase in the wet fraction content of the actual deposit. As depicted in Fig. 11, after the 3-h tests, the majority of the deposit that was exposed to HC condensation was located near the outlet section, which is consistent both with the analysis of the chemical colour image, and with the results of a previous study [68].

On the other hand, as anticipated, the deposit of case HC-100 exhibited a higher deposit density and a higher wet fraction content than the deposit of case HC-50, with a less pronounced increase of both parameters along the plate. Fig. 12 displays the results of the numerical model, which predict that a greater portion of the deposit was exposed to HC condensation during the 3-h tests, which is in agreement with the chemical colour image, that showed a larger region of the plate with a high fouling layer density.

The comparison of the results of the numerical model and the hyperspectral images confirmed that the numerical approach accurately reflected the changes in the local fouling layer density resulting from HC condensation, enabling the evaluation of the growth and development of the actual fouling layer's topography.

4. Conclusions

To enhance the simulation of the fouling layer growth caused not only by soot particles accumulation but also by hydrocarbon condensation, this research introduced a new extended numerical model. This new simulation strategy built upon previously validated numerical techniques, that only accounted for particulate matter deposition, and extended them to a new numerical tool that incorporates local hydrocarbon condensation calculations during the fouling layer formation process.

Two scenarios with varying HC concentrations in the exhaust gas were analysed to determine the thickness and density of the fouling layer at various stages of deposit formation. To verify the proper functioning of the numerical strategy, the model-predicted results were compared with experimental data obtained under the same operating conditions, computing the errors locally. Moreover, hyperspectral images of actual deposits were utilized to identify areas of varying density within the fouling layer, thereby confirming the regions where the numerical model indicated that HC condensation was a significant factor in the formation of the deposit.

Based on the results and the analysis conducted, the following conclusions were drawn:

- Regardless of the HC concentration in the exhaust gas, the morphology of the fouling layer located on the top of the ribs, that was exposed to the impact of the exhaust gas flow, was largely unaffected by the HC condensation during the entire fouling process.

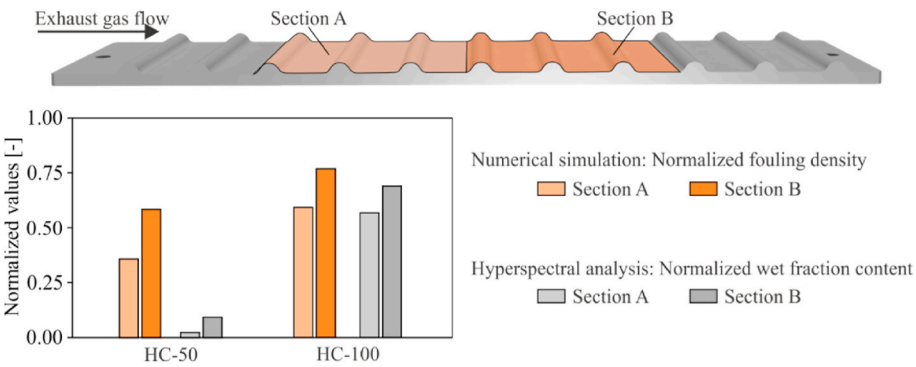

Fig. 10. Results of normalized fouling density computed with the numerical model and the normalized wet fraction content obtained through the analysis of the spectrums of the of deposits of cases HC-50 and HC-100 after 3-h tests.

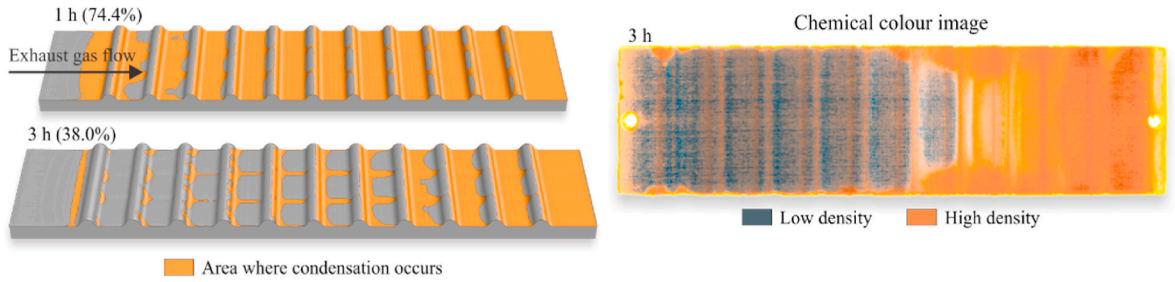

Fig. 11. CFD images of the regions where condensation occurs and chemical colour image of case HC-50 after 3-h tests. (For interpretation of the references to colour in this figure legend, the reader is referred to the Web version of this article.)

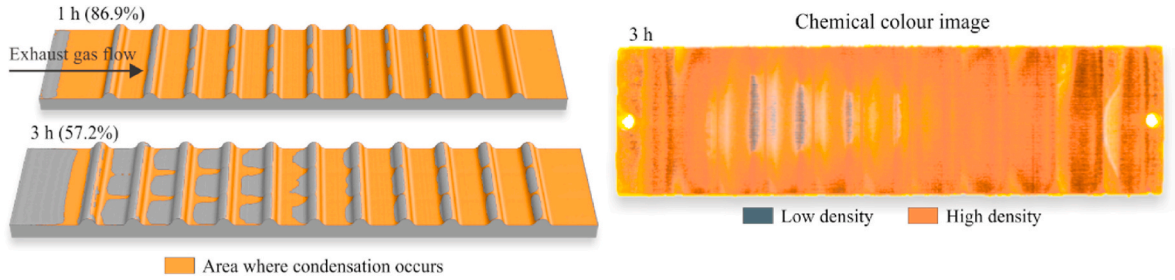

Fig. 12. CFD images of the regions where condensation occurs and chemical colour image of case HC-100 after 3-h tests. (For interpretation of the references to colour in this figure legend, the reader is referred to the Web version of this article.)

- The outlet region of the heat exchanger was significantly impacted by HC condensation, particularly in the scenario where the concentration of HC in the exhaust gas was high during the early stages of deposit formation, that leaded to the reduction of the deposit thickness.
- The local fouling thickness was reproduced with an average relative error of 18.9%, allowing to reproduce the irregular topography of the deposit.
- The evolution of local fouling density showed that as the fouling deposit progressed and inhibited HC condensation, the subsequent sublayers of the deposit exhibited a less dense structure compared to the base sublayers.
- The regions of the deposit with higher density were located in the areas between ribs, in the rib shadow zone, where the fouling layer was thinner.

In summary, the results of this study demonstrated that the newly developed wet CFD model outperforms the previous dry CFD model in predicting fouling layer formation induced by HC condensation, with an improvement of 62.2% during the most critical stages. Additionally, the wet CFD model provided deep insights into the mechanisms of condensation of volatile species in exhaust gases, contributing to the advancement of EGR systems that comply with the stringent regulations of new emission standards.

Credit author statement

J. Vence: Methodology, Modelling, Simulations, Formal analysis, Writing – original draft, Writing – review & editing, **C Paz**: Conceptualization, Methodology, Formal analysis, Supervision, Writing – original draft, Writing – review & editing, Resources, Project administration. **E. Suarez**: Supervision, Writing – original draft, Writing – review & editing; **A Cabarcos**: Formal analysis, Data curation, Experimental set up, Validation; **M. Concheiro**: Experimental Setup, Validation.

Declaration of competing interest

The authors declare that they have no known competing financial interests or personal relationships that could have appeared to influence the work reported in this paper.

Data availability

Data will be made available on request.

Acknowledgements

Authors are grateful for the financial support from the Spanish Ministry of Science and Innovation through the PDC2021-121778-100 project.

References

[1] R. Danielis, M. Scorrano, M. Giansoldati, Decarbonising transport in Europe: trends, goals, policies and passenger car scenarios, Res. Transport. Econ. 91 (2022), https://doi.org/10.1016/j.retrec.2021.101068, 101068, Mar.
[2] T. Haas, H. Sander, Decarbonizing transport in the European union: emission performance standards and the perspectives for a European green deal, Sustainability 12 (20) (2020), https://doi.org/10.3390/su12208381, 8381, Oct.
[3] S. Thiyagarajan, E.G. Varuvel, L.J. Martin, N. Beddhannan, Mitigation of carbon footprints through a blend of biofuels and oxygenates, combined with post-combustion capture system in a single cylinder CI engine, Renew. Energy 130 (2019) 1067–1081, Jan, https://doi.org/10.1016/j.renene.2018.07.010.
[4] B. Sarlioglu, C.T. Morris, D. Han, S. Li, Benchmarking of electric and hybrid vehicle electric machines, power electronics, and batteries, in: 2015 Intl Aegean Conference on Electrical Machines Power Electronics (ACEMP), 2015 Intl Conference on Optimization of Electrical Electronic Equipment (OPTIM) 2015 Intl Symposium on Advanced Electromechanical Motion Systems, ELECTROMOTION), 2015, https://doi.org/10.1109/optim.2015.7426993.
[5] J.M. Luján, A. García, J. Monsalve-Serrano, S. Martínez-Boggio, Effectiveness of hybrid powertrains to reduce the fuel consumption and NOx emissions of a Euro 6d-temp diesel engine under real-life driving conditions, Energy Convers. Manag. 199 (2019), https://doi.org/10.1016/j.enconman.2019.111987, 111987, Nov.
[6] A. Garcia, J. Monsalve-Serrano, Analysis of a series hybrid vehicle concept that combines low temperature combustion and biofuels as power source, Res. Eng. 1 (2019), https://doi.org/10.1016/j.rineng.2019.01.001, 100001, Mar.
[7] Q. Qiao, F. Zhao, Z. Liu, S. Jiang, H. Hao, Comparative study on life cycle CO2 emissions from the production of electric and conventional vehicles in China, Energy Proc. 105 (May 2017) 3584–3595, https://doi.org/10.1016/j.egypro.2017.03.827.
[8] M. Rupp, N. Handschuh, C. Rieke, I. Kuperjans, Contribution of country-specific electricity mix and charging time to environmental impact of battery electric

vehicles: a case study of electric buses in Germany, Appl. Energy 237 (Mar. 2019) 618–634, https://doi.org/10.1016/j.apenergy.2019.01.059.
[9] S.R. Dadam, R. Jentz, T. lenzen, H. Meissner, Diagnostic evaluation of exhaust gas recirculation (EGR) system on gasoline electric hybrid vehicle, in: SAE Technical Paper Series, 2020, https://doi.org/10.4271/2020-01-0902.
[10] V.S. Yaliwal, N.R. Banapurmath, M.E.M. Soudagar, A. Afzal, P. Ahmadi, Effect of manifold and port injection of hydrogen and exhaust gas recirculation (EGR) in dairy scum biodiesel - low energy content gas-fueled CI engine operated on dual fuel mode, Int. J. Hydrogen Energy 47 (10) (2022), https://doi.org/10.1016/j.ijhydene.2021.12.023, 6873–6897, Feb.
[11] S.K. Mahla, A. Dhir, K.J.S. Gill, H.M. Cho, H.C. Lim, B.S. Chauhan, Influence of EGR on the simultaneous reduction of NOx-smoke emissions trade-off under CNG-biodiesel dual fuel engine, Energy 152 (Jun. 2018) 303–312, https://doi.org/10.1016/j.energy.2018.03.072.
[12] C.B. Kumar, D.B. Lata, D. Mahto, Effect of addition of di-tert butyl peroxide (DTBP) on performance and exhaust emissions of dual fuel diesel engine with hydrogen as a secondary fuel, Int. J. Hydrogen Energy 46 (14) (2021), https://doi.org/10.1016/j.ijhydene.2020.12.129, 9595–9612, Feb.
[13] G.D. Blasio, R. Ianniello, C. Beatrice, Hydrotreated vegetable oil as enabler for high-efficient and ultra-low emission vehicles in the view of 2030 targets, Fuel 310 (2022), https://doi.org/10.1016/j.fuel.2021.122206, 122206, Feb.
[14] P.K. Senecal, F. Leach, Diversity in transportation: why a mix of propulsion technologies is the way forward for the future fleet, Res. Eng. 4 (2019), https://doi.org/10.1016/j.rineng.2019.100060, 100060, Dec.
[15] J. Ximinis, A. Massaguer, E. Massaguer, Towards compliance with the prospective EURO VII NOx emissions limit using a thermoelectric aftertreatment heater, Case Stud. Therm. Eng. 36 (2022), https://doi.org/10.1016/j.csite.2022.102182, 102182, Aug.
[16] V. Macián, J. Monsalve-Serrano, D. Villalta, Á. Fogué-Robles, Extending the potential of the dual-mode dual-fuel combustion towards the prospective EURO VII emissions limits using gasoline and OMEx, Energy Convers. Manag. 233 (2021), https://doi.org/10.1016/j.enconman.2021.113927, 113927, Apr.
[17] T. Selleri, R. Gioria, A.D. Melas, B. Giechaskiel, F. Forloni, P.M. Villafuerte, J. Demuynck, D. Bosteels, T. Wilkes, O. Simons, P. Recker, V. Lilova, Y. Onishi, M. Steffen, B. Grob, A. Perujo, R. Suarez-Bertoa, Measuring emissions from a demonstrator heavy-duty diesel vehicle under real-world conditions—moving forward to Euro VII, Catalysts 12 (2) (Feb. 2022) 184, https://doi.org/10.3390/catal12020184.
[18] S.M.A. Rahman, I.M.R. Fattah, H.C. Ong, M.F.M.A. Zamri, State-of-the-Art of strategies to reduce exhaust emissions from diesel engine vehicles, Energies 14 (6) (2021), https://doi.org/10.3390/en14061766, 1766, Mar.
[19] C. Kannan, T. Vijayakumar, Application of exhaust gas recirculation for NOx reduction in CI engines, in: NOx Emission Control Technologies in Stationary and Automotive Internal Combustion Engines, Elsevier, 2022, pp. 189–222, https://doi.org/10.1016/b978-0-12-823955-1.00007-3.
[20] C. Ciaravino, P. Ferreri, C. Pozzi, G. Previtero, F. Sapio, J. Romagnolo, Ultra-low NOx Diesel Aftertreatment: an Assessment by Simulation, Transportation Engineering, 2022, https://doi.org/10.1016/j.treng.2022.100124, 100124, Jul.
[21] X. Wang, X. Jing, J. Li, Cold start emission characteristics and its effects on real driving emission test, in: RaumFragen: Stadt – Region – Landschaft, Springer Fachmedien Wiesbaden, 2019, pp. 873–882, https://doi.org/10.1007/978-3-030-15740-1_114.
[22] H. Badshah, D. Kittelson, W. Northrop, Particle emissions from light-duty vehicles during cold-cold start, SAE Int. J. Engines 9 (3) (2016) 1775–1785, Apr, https://doi.org/10.4271/2016-01-0997.
[23] P. Bielaczyc, A. Szczotka, J. Woodburn, The effect of a low ambient temperature on the cold-start emissions and fuel consumption of passenger cars, Proc. Inst. Mech. Eng. - Part D J. Automob. Eng. 225 (9) (2011) 1253–1264, Jul, https://doi.org/10.1177/0954407011406613.
[24] K. Tanaka, T. Sakai, T. Fujino, S. Sakaida, M. Konno, K. Kinoshita, Y. Takeda, Evaluation of mechanism for EGR deposit formation based on spatially- and time-resolved scanning-electron-microscope observation, SAE Int. J. Adv. Curr. Pract. Mobility 3 (1) (2020) 150–158, https://doi.org/10.4271/2020-01-2027.
[25] K. Tanaka, K. Hiroki, T. Kikuchi, M. Konno, M. Oguma, Investigation of mechanism for formation of EGR deposit by in situ ATR-FTIR spectrometer and SEM, SAE Int. J. Engines 9 (4) (2016) 2242–2249, Oct, https://doi.org/10.4271/2016-01-2351.
[26] S. Sakaida, S. Kimiyama, T. Sakai, K. Tanaka, M. Konno, K. Kinoshita, S. Kodama, S. Mori, Effect of exhaust gas composition on EGR deposit formation, in: SAE Technical Paper Series, 2019, https://doi.org/10.4271/2019-01-2358.
[27] A.R. Razmavar, M.R. Malayeri, Thermal performance of a rectangular exhaust gas recirculation cooler subject to hydrocarbon and water vapor condensation, Int. J. Therm. Sci. 143 (Sep. 2019) 1–13, https://doi.org/10.1016/j.ijthermalsci.2019.05.006.
[28] J. Galindo, R. Navarro, D. Tarí, F. Moya, Analysis of condensation and secondary flows at three-way junctions using optical visualization techniques and computational fluid dynamics, Int. J. Multiphas. Flow 141 (2021), https://doi.org/10.1016/j.ijmultiphaseflow.2021.103674, 103674, Aug.
[29] S. Liebsch, M. Leesch, P. Zumpf, J. Jacob, R. Mehnert, P. Martin, M. Kneisel, EGR cooler fouling reduction: a new method for assessment in early engine development phase, in: SAE Technical Paper Series, 2022, https://doi.org/10.4271/2022-01-0589.
[30] C. Paz, E. Suárez, J. Vence, A. Cabarcos, Numerical modeling of fouling process in EGR system - a review, in: Environmental Change and Sustainability, Intechopen, 2020, https://doi.org/10.5772/intechopen.93062.
[31] M. Abarham, P. Zamankhan, J.W. Hoard, D. Styles, C.S. Sluder, J.M.E. Storey, M. J. Lance, D. Assanis, CFD analysis of particle transport in axi-symmetric tube flows under the influence of thermophoretic force, Int. J. Heat Mass Tran. 61 (0) (Jun. 2013) 94–105, https://doi.org/10.1016/j.ijheatmasstransfer.2013.01.071.
[32] C. Paz, E. Suárez, M. Conde, J. Vence, Development of a computational fluid dynamics model for predicting fouling process using dynamic mesh model, Heat Tran. Eng. 41 (2) (Feb. 2019) 199–207, https://doi.org/10.1080/01457632.2018.1522108.
[33] C. Paz, E. Suárez, J. Vence, A. Cabarcos, Fouling evolution on ribbed surfaces under EGR dry soot conditions: experimental measurements and 3D model validation, Int. J. Therm. Sci. 151 (May 2020), 106271, https://doi.org/10.1016/j.ijthermalsci.2020.106271.
[34] N. Epstein, Particulate Fouling of Heat Transfer Surfaces: Mechanisms and Models," *Fouling Science And Technology*, Proceedings of the NATO Advanced Study Institute, 1988, pp. 143–164, https://doi.org/10.1007/978-94-009-2813-8_10.
[35] W.B. Freeman, J. Middis, H.M. Müller-Steinhagen, Influence of augmented surfaces and of surface finish on particulate fouling in double pipe heat exchangers, Chem. Eng. Process: Process Intensif. 27 (1) (1990) 1–11, https://doi.org/10.1016/0255-2701(90)85001-K. Feb.
[36] D.Q. Kern, R.E. Seaton, A theoretical analysis of thermal surface fouling, Br. Chem. Eng. 4 (5) (1959) 258–262.
[37] M. Abarham, A Combined Modeling and Experimental Investigation of Nano-Particulate Transport in Non-isothermal Turbulent Internal Flows, University of Michigan, 2011.
[38] C.Y. Cha, B.J. McCoy, Thermal force on aerosol particles, Phys. Fluids 17 (7) (1974) 1376, https://doi.org/10.1063/1.1694899.
[39] N.B. Wood, A simple method for the calculation of turbulent deposition to smooth and rough surfaces, J. Aerosol Sci. 12 (3) (Jan. 1981) 275–290, https://doi.org/10.1016/0021-8502(81)90127-0.
[40] A. Warey, S. Balestrino, P. Szymkowicz, M.R. Malayeri, A one-dimensional model for particulate deposition and hydrocarbon condensation in exhaust gas recirculation coolers, Aerosol. Sci. Technol. 46 (2) (2012) 198–213, https://doi.org/10.1080/02786826.2011.617400. Feb.
[41] G.T. Kalghatgi, R.J. Price, Combustion Chamber Deposit Flaking, SAE Technical Paper, 2000.
[42] J. Cardot, N. Blond, P. Schmitz, Adhesion and removal of particles from surfaces under humidity controlled air stream, J. Adhes. 75 (3) (2001) 351–368, https://doi.org/10.1080/00218460108029609. Apr.
[43] J. Hoard, M. Abarham, D. Styles, J.M. Giuliano, C.S. Sluder, J.M.E. Storey, Diesel EGR cooler fouling, SAE Int. J. Engines 1 (1) (2008) 1234–1250, Oct, https://doi.org/10.4271/2008-01-2475.
[44] M. Abarham, J. Hoard, D.N. Assanis, D. Styles, E.W. Curtis, N. Ramesh, C.S. Sluder, J.M.E. Storey, Modeling of thermophoretic soot deposition and hydrocarbon condensation in EGR coolers, 2009–01–1939, SAE Int. J. Fuel. Lubric. 2 (2009) 921–931, https://doi.org/10.4271/2009-01-1939. Jun.
[45] M.J. Lance, S. Sluder, S. Lewis, J. Storey, Characterization of field-aged EGR cooler deposits, SAE Int. J. Engines 3 (2) (Oct. 2010) 126–136, https://doi.org/10.4271/2010-01-2091.
[46] H. Teng, M. Barnard, Physicochemical Characteristics of Soot Deposits in EGR Coolers, SAE Technical Papers, 2010, https://doi.org/10.4271/2010-01-0730. Apr.
[47] C. Paz, E. Suárez, J. Vence, J. Hoard, Evolution of EGR cooler deposits under hydrocarbon condensation: analysis of local thickness, roughness, and fouling layer density, Int. J. Therm. Sci. 161 (2021), https://doi.org/10.1016/j.ijthermalsci.2020.106744, 106744, Mar.
[48] M.J. Lance, J. Storey, S. Lewis, C.S. Sluder, Analysis of lacquer deposits and plugging found in field-tested EGR coolers, SAE Technical Papers 1 (Apr) (2014), https://doi.org/10.4271/2014-01-0629.
[49] Y. Lee, K.S. Hong, S. Song, K.M. Chun, K.S. Lee, S. Min, D. Chung, Evaluation of SOF Effects on Deposit Characteristics of the EGR Cooler Using a PM Generator, SAE Technical Papers, 2011, https://doi.org/10.4271/2011-01-1156. Apr.
[50] A. Salvi, J. Hoard, M. Bieniek, M. Abarham, D. Styles, D. Assanis, Effect of volatiles on soot based deposit layers, J. Eng. Gas Turbines Power 136 (11) (May 2014), 111401, https://doi.org/10.1115/1.4027460.
[51] M.S. Abd-Elhady, M.R. Malayeri, Asymptotic characteristics of particulate deposit formation in exhaust gas recirculation (EGR) coolers, Appl. Therm. Eng. 60 (1–2) (Oct. 2013) 96–104, https://doi.org/10.1016/j.applthermaleng.2013.06.038.
[52] A. Warey, A.S. Bika, A. Vassallo, S. Balestrino, P. Szymkowicz, Combination of pre-EGR cooler oxidation catalyst and water vapor condensation to mitigate fouling, SAE Int. J. Engines 7 (1) (2014) 21–31, https://doi.org/10.4271/2014-01-0636. Apr.
[53] C. Ayrault, J.S. Chang, D. Ewing, J.S. Cotton, I.E. Gerges, J. Burgers, Differential thermal analysis, thermal gravimetric analysis, and solid phase micro-extraction gas chromatography analysis of water and fuel absorption in diesel soot, J. Aerosol Sci. 41 (2) (Feb. 2010) 237–241, https://doi.org/10.1016/j.jaerosci.2009.10.006.
[54] C.S. Sluder, J.M.E. Storey, S.A. Lewis, D. Styles, J. Giuliano, J. Hoard, Hydrocarbons and Particulate Matter in EGR Cooler deposits: effects of gas flow rate, coolant temperature, and oxidation catalyst, Soc. Automotive Eng. 01–2467 (1) (2008) 1196–1204, Oct, https://doi.org/10.4271/2008-01-2467.
[55] A. Warey, D. Long, S. Balestrino, P. Szymkowicz, A.S. Bika, Visualization and analysis of condensation in exhaust gas recirculation coolers, SAE Technical Papers 2 (2013), https://doi.org/10.4271/2013-01-0540. Apr.
[56] F. Liang, M. Lu, T.C. Keener, Z. Liu, S.-J. Khang, The organic composition of diesel particulate matter, diesel fuel and engine oil of a non-road diesel generator, J. Environ. Monit. 7 (10) (2005) 983, https://doi.org/10.1039/b504728e.
[57] A.S. Mahlangu, P.W. Schaberg, M.C. Wattrus, P.B.C. Forbes, Characterisation of semi-volatile hydrocarbon emissions from diesel engines, Clean Air J. 30 (1) (2020), https://doi.org/10.17159/caj/2020/30/17672.

[58] K. Kinoshita, Y. Takeda, Y. Abe, M. Oguma, M. Konno, K. Tanaka, S. Sakaida, S. Mori, S. Kodama, Elucidation of exhaust gas recirculation deposit formation mechanism based on chemical analysis of components, Fuel 337 (2023), https://doi.org/10.1016/j.fuel.2022.127197, 127197, Apr.
[59] Ansys, Ansys Fluent Theory Guide V, 2020, 2020.
[60] M.J. Lance, Z.G. Mills, J.C. Seylar, J.M.E. Storey, C.S. Sluder, The effect of engine operating conditions on exhaust gas recirculation cooler fouling, Int. J. Heat Mass Tran. 126 (Nov. 2018) 509–520, https://doi.org/10.1016/j.ijheatmasstransfer.2018.05.069.
[61] R. Williams, S. Cook, K. Woodall, C. Clayton, M. Gee, S. Mulqueen, J. Reid, J. Rimmer, A. Ross, Development of an engine test to rate the EGR deposit formation propensity of fuels in light-duty diesel engines, SAE Int. J. Adv. Curr. Pract. Mobility 3 (1) (Sep. 2020) 337–348, https://doi.org/10.4271/2020-01-2096.
[62] Y. Itoh, T. Muruyama, Y. Zama, T. Furuhata, Effects of cooled wall temperature and HC concentration on separation behavior of PM deposit layer in an EGR cooler, in: SAE Technical Paper Series, 2019, https://doi.org/10.4271/2019-01-2357.
[63] C.S. Sluder, J.M.E. Storey, M.J. Lance, Effectiveness stabilization and plugging in EGR cooler fouling, SAE Technical Papers 1 (Apr) (2014), https://doi.org/10.4271/2014-01-0640.
[64] J. Galindo, V. Dolz, J. Monsalve-Serrano, M.A.B. Maldonado, L. Odillard, Advantages of using a cooler bypass in the low-pressure exhaust gas recirculation line of a compression ignition diesel engine operating at cold conditions, Int. J. Engine Res. (2020), https://doi.org/10.1177/1468087420914725. Apr.
[65] H. Lu, Y. Quan, A CFD study of particle deposition in three-dimensional heat exchange channel based on an improved deposition model, Int. J. Heat Mass Tran. 178 (2021), https://doi.org/10.1016/j.ijheatmasstransfer.2021.121633, 121633, Oct.
[66] M. Reißig, A. Hoppe, B. Buchholz, E. Hassel, Condensation-fouling interaction in low-temperature EGR-coolers, EDP Sci. 18 (2014), 03004, https://doi.org/10.1051/matecconf/20141803004, 2014.
[67] M.J. Lance, H. Bilheux, J.-C. Bilheux, S. Voisin, C.S. Sluder, J. Stevenson, Neutron tomography of exhaust gas recirculation cooler deposits, in: SAE Technical Paper Series, 2014, https://doi.org/10.4271/2014-01-0628.
[68] Z. Han, Y. Yao, W. Tian, X. Wu, G. He, Q. Xia, Effect of hydrocarbon condensation on fouling and heat exchange efficiency in EGR cooler, Int. J. Therm. Sci. 184 (2023), https://doi.org/10.1016/j.ijthermalsci.2022.107898, 107898, Feb.